J Surfact Deterg (2021) **24:** 897–907
DOI 10.1002/jsde.12498

ORIGINAL ARTICLE

Iron Binding in an Ethylenediaminetetracetic Acid-Based Gemini Surfactant Monolayer Film

David Sowah-Kuma[1] · Jeveria Rehman[1] · Alfred Yeboah[1] · Wei Bu[2] · Ci Yan[1] · Matthew F. Paige[1]

Received: 14 November 2020 / Revised: 30 January 2021 / Accepted: 3 February 2021

Abstract The ability of Fe^{3+} to bind to Langmuir monolayers of an N, N, N′, N′-dialkyl-N, N′-diacetate ethylenediamine gemini surfactant has been explored. Fe^{3+} in the subphase resulted in the formation of compacted, liquid-phase monolayers with a mesh-like morphology at the micron length scale in comparison with expanded, unstructured liquid-phase monolayers in the absence of iron. The response of the monolayer to subphase Fe^{3+} was different from that reported for Na^{+} and Ca^{2+} for an affiliated, shorter-tail gemini surfactant. Combined surface potential and X-ray reflectivity measurements indicated that Fe^{3+} induced minor conformational changes in the monolayer, suggesting ionic association with the head group. Direct evidence for the binding of iron was provided by total reflection X-ray fluorescence measurements, which revealed that multiple ions were associated with each head group as opposed to chelating with 1:1 stoichiometry as observed with bulk ethylenediaminetetracetic acid. Cumulative data suggest the adsorption of $Fe_x(OH)_y^{(3x-y)+}$ complexes with the monolayer surface as has been reported with other charged and uncharged monolayers.

Keywords Monolayers · Surfactants · Iron binding · X-ray fluorescence

J Surfact Deterg (2021) **24:** 897–907.

Introduction

The newly developed anionic gemini surfactants of the N, N, N′, N′-dialkyl-N, N′-diacetate ethylenediamine family, dubbed Ace(n)-m-Ace(n) in the literature, have demonstrated the ability to associate with inorganic metal ions in bulk solution and in monolayer films at the air–water interface (Lv et al., 2014; Lv and Qiao, 2015; Rehman et al., 2017a; Wattebled and Laschewsky, 2007). A representative example of these compounds, Ace(18)-2-Ace(18), is shown in Scheme 1. The association of ions with these surfactants in bulk has broadly been attributed to the chelating ability of the ethylenediaminetetracetic acid (EDTA)-based functional group that comprises the surfactant head group. Given the technological advantages of gemini surfactants over their monomeric counterparts (e.g., very low critical micelle concentrations, superior surface tension-lowering capabilities, formation of novel self-assembled structures), the association of metals with gemini surfactants holds significant potential for a variety of applications, including detergency, drug delivery, and others (Kumar and Tyagi, 2014, 2015; Menger and Keiper, 2000; Wani et al., 2019; Zana, 2002; Zhao et al., 2017), and thus, elucidating details of ion binding in these compounds is of significant technological value.

Investigations of the interactions between Ace(n)-m-Ace(n) surfactants and inorganic ions have been minimal to date and have focused primarily on Na^{+} and Ca^{2+} with Ace(12)-2-Ace(12). In their seminal work in this area, Wattebled and

Supporting information Additional supporting information may be found online in the Supporting Information section at the end of the article.

✉ Matthew F. Paige
matthew.paige@usask.ca

[1] Department of Chemistry, University of Saskatchewan, Saskatoon, Saskatchewan S7N 5C9, Canada

[2] NSF's ChemMatCARS, The University of Chicago, Chicago, IL 60637, USA

Published online: 5 April 2021
J Surfact Deterg (2021) **24:** 897–907

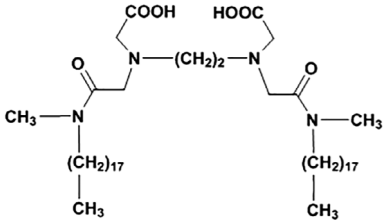

Scheme 1 Chemical structure of Ace(18)-2-Ace(18)

Laschewsky (Wattebled and Laschewsky, 2007) reported that Ace(12)-2-Ace(12) remained stable in a solution of pH 7 upon addition of Ca^{2+} ions, precipitating only when loading ratios of ~0.65 mol of Ca^{2+} per mole of surfactant head group were exceeded. For comparison, a monomeric surfactant reference compound, sodium laurate, precipitated out of solution at ion concentrations that were several orders of magnitude lower. Research on ion association in our group has focused on Langmuir and Langmuir Blodgett (LB) monolayers in which we reported on the effect of subphase Na^+ and Ca^{2+} on Ace(12)-2-Ace(12) monolayer properties, including basic pressure area (π-A) isotherm characteristics as well as film structure at air–water and air–solid interfaces (Rehman et al., 2017a). The presence of either cation in the subphase resulted in the significant expansion of the monolayer film in comparison with an ion-free subphase, with Ca^{2+} inducing a greater film expansion than Na^+. π-A isotherm data were used to estimate ion-to-surfactant binding stoichiometry (N = 1 and N = 0.5 for Na^+, Ca^{2+}, respectively) and apparent association constant values; binding stoichiometry was the same as is typically observed for simple (two-tailed) phospholipids, while association constant values were smaller. Brewster angle microscope (BAM) measurements revealed the formation of multimolecular aggregates in the presence of ions, which were likely agglomerations of the surfactant bound to the metal.

The association of trivalent ions with surfactant molecules is more complex compared to most mono- or divalent ions (e.g., see (Aroti et al., 2004; Shah and Schulman, 1965) and the references therein) in part because of the potential for forming coordinate covalent bonds between the transition metal ions and surrounding ligand molecules in bulk solution (Tyrode and Corkery, 2018; Wang et al., 2014, 2016; Wen et al., 2016). More broadly, interactions between trivalent ions, and iron in particular, with charged surfactant interfaces is of interest because of their importance in membrane-based biomineralization processes, as well as their relevance in controlling the interaction between metal-based nanomaterials and self-assembled ionic surfactants that comprise nanoparticle coatings (Arakaki et al., 2003; Kang et al., 2002). Studies have also been carried out on protein-based systems, and evidence has been obtained for the formation of complexes between the functional groups of protein molecules and metal ions in the bulk and at the interface (see (Lopez-Moreno et al., 2017; Mirabello et al., 2016; Uebe and Schueler, 2016) and others). Sung et al. (2018) have recently investigated the binding between a Langmuir monolayer consisting of fatty acid molecules and two trivalent ions, Fe^{3+} and La^{3+}. Using sum frequency generation vibrational spectroscopy, high binding energies were found to exist between the carboxylic acid head group (both protonated and neutral forms) and Fe^{3+} ions and $Fe(OH)_x^{+3-x}$ complexes, which were associated with the half-filled d-orbitals of iron. Furthermore, the measurements indicated that iron bound to the fatty acid head groups primarily as hydroxide complexes, whereas La^{3+} ions (filled d-orbital) bound as "bare" ions to the deprotonated head group and behaved in a manner similar to previously studied monovalent and divalent ions. Wang et al. (Wang et al., 2014) have also investigated the adsorption of Fe^{2+} and Fe^{3+} to monolayers of arachidic acid and dihexadecyl phosphate (DHDP) using a combination of X-ray-based methods; they reported that the quantity of Fe^{3+} bound to either monolayer was largely independent of the charge density of either interface, and the amount of bound Fe^{3+} was more than one-third per surfactant head group. Based on interface-sensitive X-ray absorption near-edge spectra measurements, the authors also noted that the ions were "chemically" bound to the surfactant head groups (i.e., a Stern layer) as opposed to loosely associated.

In the current study, the impact of subphase iron on surfactant monolayer properties has been investigated with a trivalent ion, Fe^{3+}, and the gemini surfactant Ace(18)-2-Ace(18). With the half-filled Fe^{3+} d-orbital and a surfactant head group bearing similarities to EDTA, the surfactant is expected to show significant binding with Fe^{3+}, and the impact of this on monolayer properties, including pressure area compression isotherms, micron-scale film morphology, and surface dipole moment, is explored. In addition, we have directly measured the extent of iron binding to the monolayers through synchrotron-based X-ray fluorescence measurements and assessed binding stoichiometry at the air–water interface.

Experimental Section

Chemicals and Substrates

$FeCl_3$ (reagent grade, 97%) and chloroform (spectrophotometric grade) were purchased from Sigma Aldrich (Oakville, Ontario, Canada), and HCl (ACS grade) was purchased from EMD Merck. We have reported the synthesis, purification, and characterization of Ace(18)-2-Ace(18) previously (Rehman et al., 2019). Stock solutions (1 mM) of Ace(18)-

2-Ace(18) were prepared by dissolving the solid surfactant in chloroform. For deposition experiments, microscope glass slide coverslips (VWR) were used as substrates. The coverslips were rinsed with ethanol and, after drying with nitrogen, cleaned in a plasma cleaner (Harrick Plasma) for approximately 30 min before use.

Monolayer Preparation, Compression Isotherms, and Surface Potential Measurements

Langmuir and Langmuir Blodgett films were prepared on a Langmuir trough (KSV Nima) equipped with a Wilhelmy plate balance using filter-paper plates. The trough was cleaned thoroughly before each measurement. π-A isotherms were collected for Ace(18)-2-Ace(18) monolayers at room temperature using ultrapure water (MilliQ; resistivity = 18.2 $M\Omega \cdot cm^{-1}$) whose pH had been adjusted to 3.7 by adding trace amounts of 1 M HCl as a subphase. For iron-enriched subphases, $FeCl_3$ was dissolved in ultrapure water, and the pH of each solution was adjusted to 3.7 by the addition of 1 M HCl. To prepare monolayers, 50 μL of stock Ace(18)-2-Ace(18) solution was spotted on the subphase surface using a Hamilton syringe, and the film was allowed to equilibrate for ~15 min before compression. Films were compressed at a rate of 20 mm min^{-1} (approximately 5.0 $Å^2$ molecules min^{-1}). Surface potential measurements were taken using a commercial vibrating metal plate probe (KSV Nima) mounted on a Langmuir trough. LB films were deposited onto glass coverslips at a surface pressure π = 30 mN m^{-1} at a deposition rate of 10 mm min^{-1}.

Microscopy Measurements

Atomic force microscope (AFM) measurements were carried out in tapping mode on a Dimension Hybrid Nanoscope system (Veeco). Silicon probes with spring constants in the range of 10–100 N m^{-1} and resonance frequencies between 288 and 338 kHz were used. Samples were imaged at a scan rate of 0.45 Hz and a resolution of 512 pixels per line.

BAM imaging was performed at the air–water interface on a Langmuir trough equipped with a BAM system (Ultra BAM, KSV Nima). The BAM system used a 658 nm laser for illumination, and all images were collected at 20 frames s^{-1}. The diffraction-limited resolution of the instrument was ~2 μm.

X-Ray Reflectivity and Total Reflection X-Ray Fluorescence Measurements

X-ray reflectivity (XR) and total reflection X-ray fluorescence (TRXF) measurements were carried out on the liquid surface scattering spectrometer of sector 15-ID-C (NSF's ChemMatCARS) at the Advanced Photon Source (Argonne National Laboratories). The spectrometer was equipped with a Langmuir trough with a single movable barrier, all encased in a sealed chamber mounted on a vibration isolation pad. The liquid footprint inside the trough had dimensions of 42.0 cm (length) × 8.9 cm (width) × 0.7 cm (depth). For TRXF measurements, an $[Fe^{3+}]$ = 50 mM subphase was used as a reference solution. Monolayer films were prepared by spotting the surfactant solution onto the subphase in the trough, and the chamber was purged with He to minimize X-ray beam scattering by air and to minimize potential damage to the film caused by the incident beam. The X-ray beam intensity was adjusted to avoid film damage over the time course of the experiments. A monochromatic beam of X-rays with energy of 10 keV (λ = 1.23984 Å) was directed onto the surface of the subphase using a Ge (111) steering crystal. For XR measurements, reflected X-rays were collected on a Pilatus 100 K X-ray detector (Dectris) as a function of out-of-plane (q_z) scattering vector. Fluorescence signals were collected normal to the surface on a multicathode energy-dispersive X-ray detector (SII Nano Technology USA, Inc.) at small incident beam angles (α_i) as a function of the out-of-plane (q_z) scattering vector. Angular-dependent fluorescence measurements were used to extract the surface ion concentration (ions per unit area) using the fitting approach described by Bu et al. (Bu et al., 2014).

Results and Discussion

For the monolayer experiments, a combination of acid–base properties of Ace(18)-2-Ace(18) (pKa_1 = 5.6, pKa_2 = 9.3, corresponding to protonation–deprotonation of the head group nitrogens) and the solubility of iron salts dictated which subphase conditions could be investigated. Maximal binding of cationic iron to Ace(18)-2-Ace(18) is anticipated for the fully deprotonated surfactant, but iron hydroxides precipitate under these conditions. Because of this, we empirically identified a subphase pH and an Fe^{3+} concentration range for which there was no detectable precipitate formation but where significant ion binding was still observed by X-ray fluorescence (*vide infra*). These were identified as pH = 3.7 and $[Fe^{3+}]$ = 0.0–1.0×10^{-1} mM, and these conditions were used for further experiments. It should be noted that, under these conditions, the speciation of the nominal $Fe^{3+}_{(aq)}$ subphase is complex; because of iron's Lewis acidity, a significant fraction will coexist as $FeOH^{2+}_{(aq)}$ and $Fe(OH)_{2\ (aq)}$ (Stefansson, 2007). Furthermore, the addition of HCl for pH adjustment will also complicate the issue, potentially promoting the formation of chloride-enriched complex ions, although this effect becomes more important at higher iron chloride concentrations

(Persson, 2018). For the sake of simplicity, the subphase will be referred to as $Fe^{3+}_{(aq)}$ in the remainder of the text. At this pH, Ace(18)-2-Ace(18) can reasonably be assumed to be zwitterionic (head group nitrogens protonated, carboxylic acids deprotonated). While we cannot confirm this experimentally using titration because the compound precipitates at low pH, the pKa values for the carboxylic acid groups in EDTA (Harris, 2010) are ~2.0 and 2.7, and thus, we will proceed based on the assumption of a zwitterionic head group.

π-A isotherms for Ace(18)-2-Ace(18) monolayers were measured as a function of Fe^{3+} subphase concentrations and are shown in Fig. 1. Isotherms were consistent with those reported previously for pure water and ion-containing subphases (Rehman et al., 2017a) and consisted of a smoothly increasing curve with no discernible phase transitions and a well-defined film collapse. Compressibility modulus plots ($C_s^{-1} = -MMA(d\pi/dMMA)_T$ vs. π) for monolayers at the

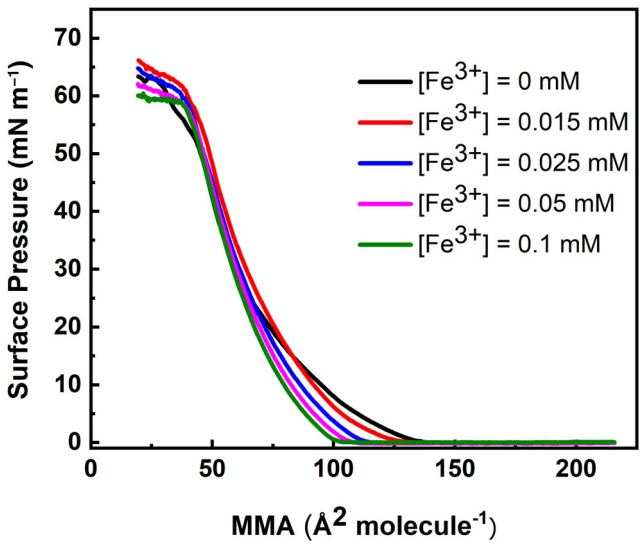

Fig. 1 π-A isotherms for Ace(18)-2-Ace(18) monolayers as a function of subphase [Fe^{3+}] at pH 3.7 and 21 °C

Table 1 Summary of monolayer properties extracted from π-A isotherms for Ace(18)-2-Ace(18) as a function of sub-phase [Fe^{3+}]

[Fe^{3+}] (mM)	A_0[a] (Å^2/molecule)	A_c[b] (Å^2/molecule)	π_c[c] (mN m^{-1})	$C_s^{-1}{}_{max}$[d] (mN m^{-1})
0	83.5 ± 0.2	19.4 ± 0.1	63.3 ± 0.3	84.4 ± 0.1
1.5×10^{-2}	83.2 ± 0.4	19.6 ± 0.4	66.2 ± 0.4	87.2 ± 0.4
2.5×10^{-2}	81.5 ± 0.3	19.4 ± 0.3	64.8 ± 0.1	80.6 ± 0.3
5.0×10^{-2}	80.3 ± 0.2	19.4 ± 0.3	62.1 ± 0.1	86.8 ± 0.2
1.0×10^{-1}	78.5 ± 0.1	19.4 ± 0.5	60.0 ± 0.1	86.7 ± 0.4

[a]Determined by fitting a straight line to the most steeply increasing region of isotherm and extrapolating to zero.

[b]Mean molecular area at film collapse.

[c]Film collapse pressure.

[d]Maximum observed compressibility modulus.

various Fe^{3+} concentrations were calculated from the isotherms and are reported as Supporting Information.

Previously reported grazing incidence X-Ray diffraction measurements of Ace(18)-2-Ace(18) monolayers indicates that these surfactants form liquid (nondiffracting films) at the air–water interface at all surface pressures, likely because the bulky head groups pack poorly (Rehman et al., 2019) and the lack of discontinuities in the isotherms is consistent with the absence of liquid-to-solid or similar phase transitions. The maximal values for C_s^{-1} extracted from the isotherms are consistent with liquid-state films under all measurement conditions. Key properties of the isotherms and their changes as a function of subphase ion concentration are summarized in Table 1. The limiting area for the films (A_0 estimated by extrapolating the steeply rising region of the isotherm to π = 0 mN m^{-1}) on pure water was 83 Å^2, which is significantly higher than a typical monomeric surfactant (e.g., stearic acid, A_0 = 20.9 Å^2; see (Islam et al., 2008)) and slightly larger than that of the shorter-chain gemini variant Ace(12)-2-Ace(12) (A_0 = 61 Å^2) (Rehman et al., 2017a). The larger limiting area of Ace(18)-2-Ace(18) in comparison with stearic acid can be attributed to the larger head group cross section of the molecule. The larger value in comparison with Ace(12)-2-Ace(12) is consistent with previous X-ray reflectivity measurements, which suggest that the Ace(18)-2-Ace(18) tends to "flatten" on the subphase surface (Rehman et al., 2019).

Film collapse areas (A_c) and collapse pressures (π_c) showed minimal variation with Fe^{3+} content, and there was no significant change in the shape of the isotherms as a function of iron concentration. However, isotherms shifted systematically to smaller mean molecular areas (film condensation) as the Fe^{3+} concentration in the subphase increased. The greatest film condensation was observed for the highest iron concentration; the maximum condensation was ~5% as estimated from the difference in the limiting area of Ace(18)-2-Ace(18) on pure water. There is a diverse set of responses of monolayers to subphase ions reported in the literature (Leontidis et al., 2014), but a common cause of film condensation is simple screening of charge from ionized head groups. For example, more condensed films are commonly observed for simple fatty acids with ionic subphases compared to pure water subphases (Brzozowska et al., 2013; Petty, 1996). Wang et al. have reported similar responses for dipalmitoyl phosphatidylcholine monolayers on the Fe^{3+} subphase, where films were condensed in the liquid expanded (LE) phase as the Fe^{3+} subphase concentration was increased (Wang et al., 2016). As noted above, the subphase pH is approximately two orders of magnitude smaller than the bulk solution pKa_1 (which corresponds to protonation of the nitrogen head group) for the surfactant. While the pKa values in monolayers will differ from the bulk, we can reasonably anticipate that the surfactant head

group will be zwitterionic (both carboxylic acid groups deprotonated and both nitrogens protonated), and thus, charge screening is certainly a viable cause of film compaction. However, one most also consider the possibility that ion binding leads to a large conformational change in the head group, which might also result in perturbation to the monolayer film structure. At this pH, EDTA in bulk solutions will still chelate iron, albeit with less affinity than at higher pH, and it is reasonable to postulate that the association between the head group and the metal ion in solutions might be accompanied by a structural change that reflects this type of association. Thus, additional characterization approaches were used to further assess the impact of subphase Fe^{3+} on the film structure.

Surface potential (SP) measurements were used to probe the orientation of the surfactant's dipole moment at the air–water interface as a function of Fe^{3+} concentration, with experimental results shown in Fig. 2. SP values and corresponding surface dipole moments ($\mu_\perp$) calculated using the Helmholtz relation ($\mu_\perp = \epsilon_0\ \Delta V\ A$; ϵ_0 is vacuum permittivity, ΔV is the experimentally measured difference in SP, A is area) are summarized in Table 2. For the tabulated values, a fixed area of 75 $Å^2$·molecule^{-1} was selected.

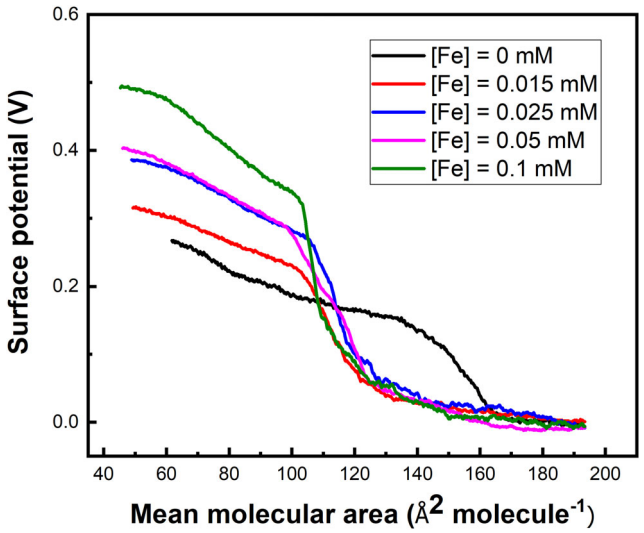

Fig. 2 Surface potential plots for Ace(18)-2-Ace(18) as a function of subphase [Fe^{3+}] at pH 3.7 and temperature 21 ± 0.5 °C

Table 2 Surface potential (SP) data for Ace(18)-2-Ace(18) on Fe^{3+} subphase

[Fe^{3+}] (mM)	SP[a] (V)	$\mu_\perp$ (D)
0	0.23	0.46
1.5×10^{-2}	0.27	0.53
2.5×10^{-2}	0.34	0.68
5.0×10^{-2}	0.35	0.70
1.0×10^{-1}	0.42	0.84

[a]Measured at 75 Å·molecule^{-1}.

Measured SP values increased as a function of film compression for all monolayer films, regardless of subphase composition, consistent with orienting the surfactant's molecular dipole moment (which we consider pointing toward the head group) normal to the water surface as the film was compressed. Absolute SP values were comparable with those reported previously for Ace(12)-2-Ace (12) monolayers, indicating that increasing the alkyl tail length does not substantially alter the molecular dipole moment as might be reasonably expected; the primary influence on the dipole moment will be from the head group and functional groups immediately adjacent to this. SP compression curves were generally unremarkable, but of particular interest was that the curve on pure water was significantly different for monolayer films on Fe^{3+} in the subphase; the potential on pure water increased at a significantly larger mean molecular area than the others. This result was repeatable over many replicate measurements, which indicates that the presence of Fe^{3+} significantly changes the orientation of the surfactant's dipole moment over that observed on pure water. For more compacted films (taken at an area of 75 $Å^2$ molecule^{-1}), the impact of Fe^{3+} was particularly apparent. As the concentration of Fe^{3+} was increased in the subphase, an increase in the SP was observed, indicating a tendency of the dipole moment toward normal orientation with respect to the surface. Providing a molecular-level interpretation of the SP on the ion-containing subphase is more complex than that on pure water alone. For the first approximation, the overall SP can be modeled as a combination of dipole orientation effects, as well as an electric double-layer contribution from the association of ions with the charged monolayer. As noted above, the net head group charge should be zero (zwitterionic) at the pH used, and thus, the latter effect should be minimal, but nonetheless, some limiting case order-of-magnitude calculations (0.5% surface ionization) were carried out to assess the importance of ion binding on SP. We have modeled the electric double-layer potential for a 3:1 ($FeCl_3$) electrolyte using the method described by Casper et al. (Casper et al., 2015) as a function of film compression and subphase Fe^{3+} concentration (see Supporting Information). These calculations showed that the change in electric double-layer contribution to the measured SP is negligible over the experimental compression range used here, and in combination with the SP being null at the beginning of each compression experiment, the measurements indicate that the change in measured SP can be attributed to changes of the surfactant dipole moment. The changes in dipole moment are substantive; at a reference area of 75 $Å^2$ molecule, the dipole moment is almost twice that reported on pure water. We interpret this as meaning that the addition of Fe^{3+} to the subphase significantly reorients the dipole moments at the air–water interface.

Unraveling precisely what molecular-level structural changes occur in the monolayer is challenging based on the data given here. A fundamental limitation of the SP measurements described here is that one cannot assume that the surfactant's molecular dipole moment remains fixed as the concentration of subphase Fe^{3+} increases and that changes in $\mu_{\perp}$ result from simple reorientation of a rigid rod-like molecule. While this approach generally works well for rigid, rod-like surfactants like short-chain fatty acids, Ace(18)-2-Ace(18) has the potential for more significant conformational flexibility. As noted in the isotherm data, binding of the metal ion might result in a significant conformational change in the structure of the molecule, which would also perturb the measured SP. We note that the XR measurements reported previously (Rehman et al., 2019) suggest that Ace(18)-2-Ace(18) on pure water has a disordered tail group region, and the head group adopts a "flattened" conformation, similar to what is reported for cationic alkyl ammonium gemini surfactants with an appropriately sized spacer group (Alami et al., 1993). Thus, we have carried out additional structural characterization measurements on the films in the presence of Fe^{3+} to supplement the SP measurements.

To assess micrometer-scale film morphology, films were visualized at the air–water interface using BAM. Figure 3 shows the BAM images for Ace(18)-2-Ace(18) monolayer films as a function of Fe^{3+} subphase concentrations at $\pi = 1$ mN m^{-1}. Comparable results were obtained at higher pressures ($\pi = 5$ mN m^{-1}; Supporting Information), but at significantly greater film compression ($\pi > 10$ mN m^{-1}), the features observed in the films merged to the point of becoming unresolvable at the resolution of the instrument. BAM images of pure Ace(18)-2-Ace(18) films on a subphase of pure water consisted of minimally reflective spots that were several microns in diameter (Fig. 3a). Control measurements of pure water or Fe^{3+}-enriched subphases in the absence of surfactant were featureless, indicating that these domains were aggregates of surfactant and that the pure surfactant had a weak tendency to form aggregates in the absence of subphase cations.

Films on Fe^{3+} containing subphases showed a significantly different morphology compared to the pure water subphase (Fig. 3b–e). Films consisted of low reflectivity (dark) elliptical domains dispersed in a highly reflective mesh-like structure. The low-reflectivity, elliptical domains were minimally structured and heterogeneous in size, typically ranging from tens to hundreds of microns in diameter. There was no discernible trend in terms of the relative number and size of domains as a function of Fe^{3+} subphase concentration. We interpret these images as being consistent with film condensation induced by subphase Fe^{3+}; the regions of higher reflectivity correspond to condensed patches of surfactant, likely associated with iron species, but the films have not been sufficiently compacted for uniform

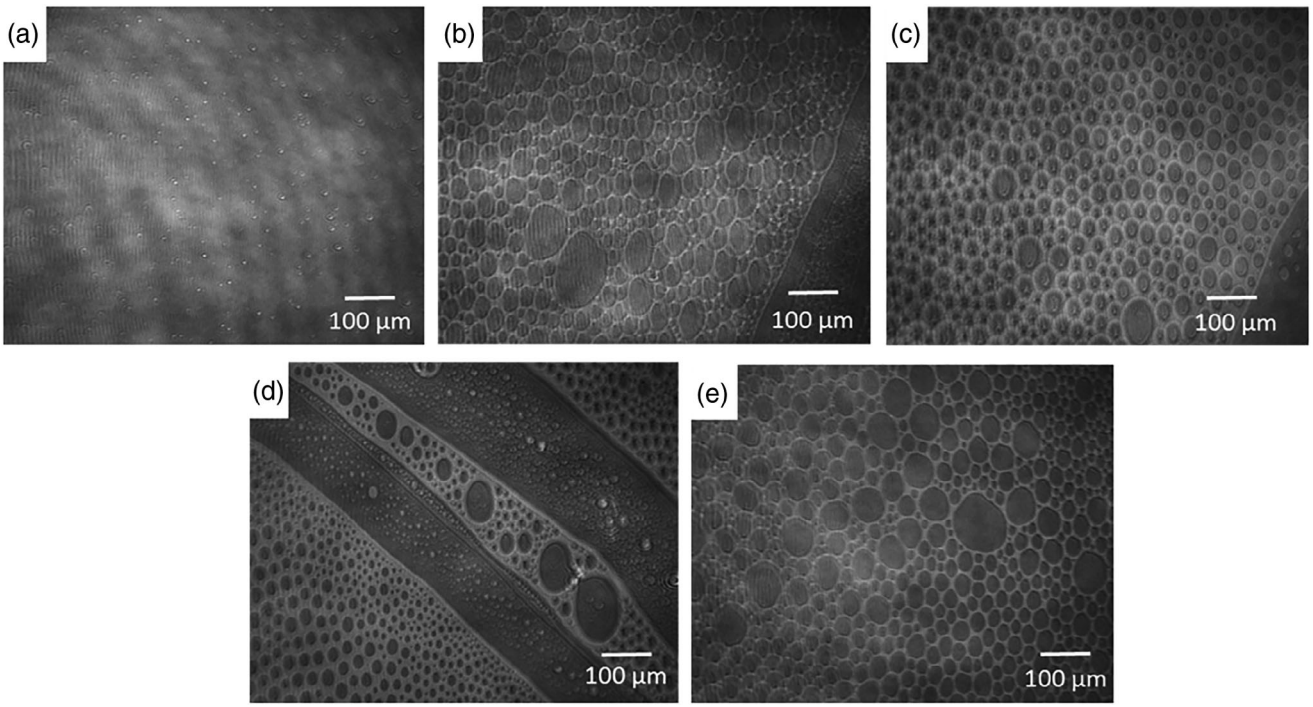

Fig. 3 BAM images of Ace(18)-2-Ace(18) monolayers as a function of concentration of [Fe^{3+}] in subphase at $\pi = 1$ mN m^{-1} and temperature 21 ± 0.5 °C. (**a**) [Fe^{3+}] = 0 mM, (**b**) [Fe^{3+}] = 1.5×10^{-2} mM, (**c**) [Fe^{3+}] = 2.5×10^{-2} mM, (**d**) [Fe^{3+}] = 5.0×10^{-2} mM, and (**e**) [Fe^{3+}] = 1.0×10^{-1} mM

coverage; thus, there are empty (low reflectivity) regions on the subphase. This assignment is in good agreement with our previous observations for the Ace(12)-2-Ace (12) system; the shorter tail system showed precisely opposite behavior to that observed here, in that it formed expanded films in the presence of Na^+ and Ca^{2+}, and the

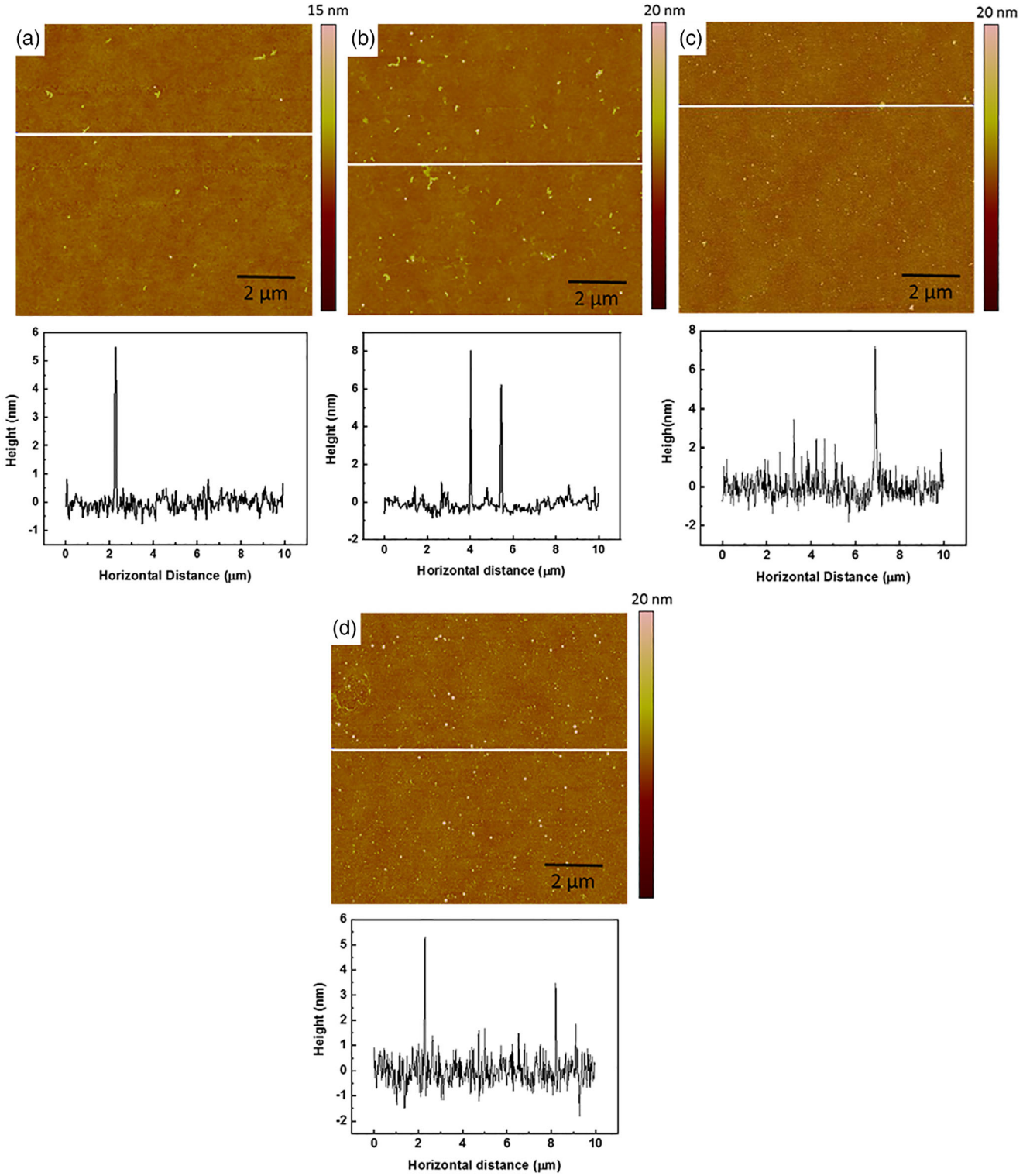

Fig. 4 AFM height images (10 μm × 10 μm) and corresponding cross-sectional analysis of Ace(18)-2-Ace(18) as a function of concentration of $[Fe^{3+}]$ in subphase at π = 30 mN m^{-1} and temperature 21 ± 0.5 °C. (**a**) $[Fe^{3+}] = 1.5 \times 10^{-2}$ mM, (**b**) $[Fe^{3+}] = 2.5 \times 10^{-2}$ mM, (**c**) $[Fe^{3+}] = 5.0 \times 10^{-2}$ mM, and (**d**) $[Fe^{3+}] = 1.0 \times 10^{-1}$ mM

Table 3 X-ray reflectivity and total reflection X-ray fluorescence fitting parameters for Ace(18)-2-Ace(18) on Fe^{3+} subphase measured at $\pi = 20$ mN m^{-1}

[Fe^{3+}] (mM)	Head layer length (Å)	Tail layer length (Å)	Surface ion concentration (ions $Å^{-2}$)	Fe^{3+} ions per head group
0	10.6 ± 0.3	14.9 ± 0.2	—	—
1.5×10^{-2}	9.1 ± 0.2	13.2 ± 0.2	0.037 ± 0.002	2.8 ± 0.1
2.5×10^{-2}	10.0 ± 0.3	11.3 ± 0.1	0.049 ± 0.002	3.7 ± 0.2
1.0×10^{-1}	10.7 ± 0.3	11.2 ± 0.1	0.069 ± 0.003	5.2 ± 0.2

BAM images consisted of occasional high-reflectivity aggregates dispersed on a continuous dark phase (Rehman et al., 2017a).

To further elucidate the structures of the films, monolayers prepared at varying Fe^{3+} subphase concentrations were deposited onto glass substrates (at $\pi = 30$ mN m^{-1}) and imaged using AFM. Images of films deposited as a function of subphase Fe^{3+} concentration are shown in Fig. 4, and an image of a film deposited from a pure water subphase is reported as Supporting Information. For all conditions investigated, including depositions in the absence of Fe^{3+}, film transfer ratios were > 1, indicating that more than a single monolayer of material was deposited. The large transfer ratios indicate that the films do not retain good structural integrity upon transfer, and thus, we interpret the AFM results cautiously. Films deposited from pure water consisted of a smooth layer dotted with occasional pinhole defects, while films deposited from Fe^{3+} subphases consisted of a smooth layer with numerous heterogeneous aggregates dispersed across the sample. Cross-sectional analysis of these aggregates (Fig. 4) yielded heights that were ~ 5–7 nm, which is significantly larger than the estimated length for a fully extended Ace(18)-2-Ace(18) molecule (~2 nm, estimated from MMFF molecular mechanics calculations, Spartan 2018). We (qualitatively) observed a larger number of aggregates in the films prepared from the highest Fe^{3+} concentration samples and thus interpret the aggregates to consist of Ace(18)-2-Ace(18) associated with Fe^{3+} species, the quantity of which increases with Fe^{3+} concentration. We revisit the nature of the surfactant Fe^{3+} species in the Discussion section of this manuscript.

XR was used to examine monolayer thickness at the air–water interface in the presence and absence of Fe^{3+} (at $\pi = 20$ mN m^{-1}), with normalized XR curves (R/R_f vs. q_z, where R is reflectivity and R_f is the Fresnel reflectivity) reported in Fig. S3. Resulting electron density profiles were fit using a standard two-slab model in which one slab of electron density corresponds to the monolayer head group and the second slab to the tail group; fitting data are summarized in Table 3. The overall film thickness and

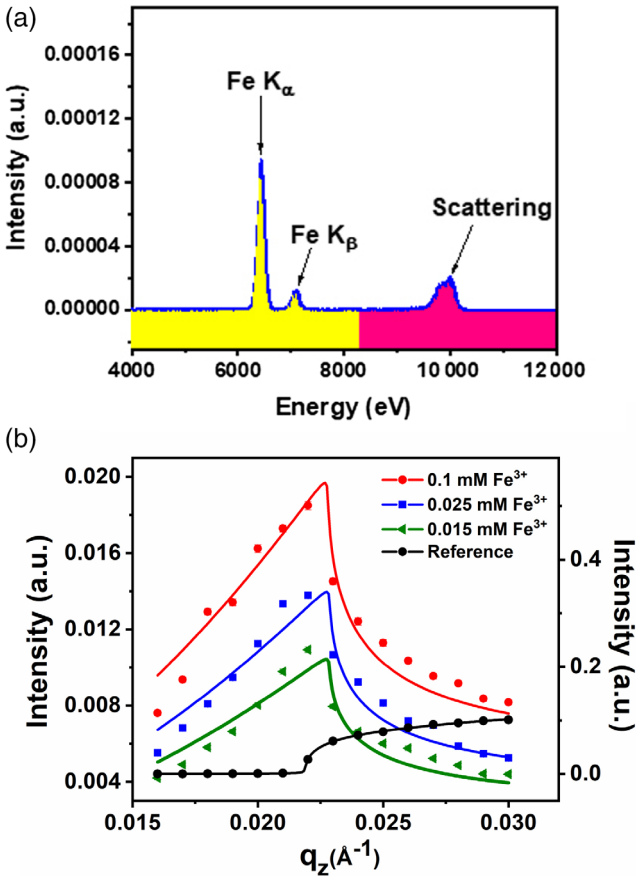

Fig. 5 (**a**) Fluorescence spectrum from the interface between Ace (18)-2-Ace(18) and Fe^{3+} subphase ($q_z = 0.018$ $Å^{-1}$, [Fe^{3+}] = 0.25×10^{-4} M, $\pi = 20$ mN m^{-1}). (**b**). Integrated fluorescence intensity as a function of q_z for Ace(18)-2-Ace(18) and Fe^{3+}-containing subphases ($\pi = 20$ mN m^{-1}, 6.4 keV). The points are experimentally measured intensities, and the solid lines are the modeled fit determined as described by Bu et al. (Bu et al., 2014). The vertical scale on the right refers to the reference sample intensity signal. The reference subphase consisted of [Fe^{3+}] = 50 mM

slab-fitting results for the monolayer on pure water were comparable with the previously measured values for Ace (18)-2-Ace(18), and the tail layer length was greater than that of the shorter Ace(12)-2-Ace(12) surfactant, as expected (Rehman et al., 2017b, 2019). The key observation from film thickness measurements was that a small (~ 4 Å) but significant decrease in tail layer length was observed when switching to an Fe^{3+}-enriched subphase. Similar tail layer lengths for all Fe^{3+} concentrations were calculated, and we were not confidently able to extract any particular concentration-dependent trends with regard to thickness. Nonetheless, there was a clear alteration in the film structure induced by the interaction of the monolayer with Fe^{3+}. It is somewhat surprising that binding would have minimal effect on the head group thickness and rather perturbs the effective tail group thickness; we naively assumed that binding to the Ace(18)-2-Ace(18) head would

result in substantial changes, particularly if the iron formed a chelate, but clearly, this is not the case. The relatively small change in thickness of the tail region suggests that the majority of the change in dipole moment observed in the SP measurements is simply caused by the molecules adopting a more vertical orientation. This minimal change in the head group region suggests that the Fe^{3+} is not chelated but is, rather, nonspecifically bound to the monolayer. Furthermore, we speculate that the nonspecific binding effectively "levers" the two tail chains apart, resulting in a lower average tail chain thickness. The XR-determined tail length is shorter than expected for a fully extended alkyl chain (~ 18 Å), suggesting that there is disorder (and possibly flexibility) in the tail region in the absence of Fe^{3+}, which might allow for these conformational changes to occur. However, we are unable to definitively account for this effect and will explore it further in the future. However, additional insight into the Fe^{3+}–surfactant binding interaction could also be obtained using X-ray fluorescence techniques, as detailed below.

The amount of Fe^{3+} bound to the Ace(18)-2-Ace (18) monolayers was measured using TRXF, which provides information about elemental distribution across layered structures directly at the air–water interface.(Kumar and Tyagi, 2015) Figure 5a shows the fluorescence spectra from the interface between Ace(18)-2-Ace(18) and an Fe^{3+} subphase ($[Fe^{3+}] = 0.25 \times 10^{-4}$ M). Fe K_α emission was observed at 6.4 keV, and the Fe K_β emission was observed at 7.1 keV, with typical X-ray and Compton scattering observed at their expected energies (Albert and Douglas, 2020). This indicates the presence of Fe^{3+} ions at the air–water interface. Measurements of an iron-enriched subphase without the surfactant showed negligible Fe fluorescence at the interface, indicating that the surfactant monolayer draws metal ions to it from bulk solution. TRXF can be used to quantify the amount of surface-bound metal ions, expressed as interfacial area per metal ion. The process for extracting the data is described in detail by Bu et al. (Bu et al., 2014), but in brief, the dependence of fluorescence intensity on the X-ray angle of incidence for a given subphase ion concentration is measured, and the bound ion quantity is extracted from the data by fitting the angle-dependent data to an appropriately parameterized model.

Plots of integrated fluorescence as a function of q_z for the monolayer systems (Fig. 5b) show a sharp transition at $q_z \sim 0.022$ Å^{-1} and have shapes consistent with a Fresnel transmission curve. The peak sharpness indicates negligible interfacial curvature, and the shape points to a signal that is dominant at the interface over the bulk. Closely affiliated systems reported in the literature, including Fe^{3+} ions with DHDP and Fe^{3+} with arachidic acid, exhibited similar fluorescence response (Fig. 4b). A standard reference sample consisting of a $[Fe^{3+}] = 50$ mM solution in the absence of a surfactant monolayer yielded an entirely different angular response (black curve), the shape of which was characteristic of fluorescence emission from bulk solution. Curve fitting based on the assumption of a uniform plane of metal ions at the interface was carried out and yielded surface ion concentrations, which were converted into ions per Ace (18)-2-Ace(18) head group using the π-A isotherm data. Results are summarized in Table 3.

For all conditions, ion to head group ratios that were greater than one were observed, which is consistent with the proposed model of nonspecific association of ions to the monolayer as opposed to one-to-one chelation. This general result is consistent with several reports in the literature of iron binding to various charged or uncharged surface layers. Of particular note is Wang et al.'s report on interactions of Fe^{3+} ions with DHDP which suggested that iron hydroxide (ferrihydrite) complexes were associating with the interface and that binding was largely independent of the surface charge density (Wang et al., 2014). Further support for this was provided by a follow-up study in which the authors reported the adsorption of iron (III) to a charge neutral zwitterionic template of phosphatidylcholine (PC) (Wen et al., 2016). The authors proposed that the iron hydroxide clusters, broadly described as $Fe_x(OH)_y^{(3x-y)+}$—although, again, the precise speciation is complex—that form in solution under their experimental conditions (pH 3, 100 mM KCl) bind covalently to PC, which resulted in a large number of ions per surfactant head group (~3). A similar effect can reasonably explain the large ion–surfactant binding stoichiometry we observe with the Ace(18)-2-Ace (18) system, as well as the ability of iron-containing species to adsorb to the nominally zwitterionic surface.

Furthermore, the effect agrees with the cumulative microscopy data. Metal hydroxide clusters bound to a surfactant would certainly provide excellent reflectivity contrast in air–water interfacial BAM images, and the results reported above are consistent with this. In terms of the AFM data, while the poor transfer ratios preclude meaningful quantitative analysis, the aggregate diameters observed were in the range of 5–7 nm, which is typical of ferrihydrite nanocrystals (Michel et al., 2007). Cumulatively, the weight of evidence supports the formation and adsorption of these complexes to the Ace(18)-2-Ace(18) monolayer at the air–water interface, although the precise chemical composition of the surface-bound clusters would require future studies with a surface-sensitive spectroscopic probe (e.g., XANES). A further point of interest here is the comparatively large quantity of iron bound per head group in this system (five ions per head group at the highest subphase Fe^{3+} concentration used). For technical applications in which high Fe^{3+} loading levels onto surfactants are desirable, for example, micronutrient delivery, encapsulation, or metal nanoparticle synthesis, the capacity for metal binding

exhibited for the EDTA-like head group might be a very useful, and further chemical refinements to explore structure-binding capacity relationships in this class of compounds are ongoing.

Conclusion

Ace(18)-2-Ace(18) surfactant monolayers have been demonstrated to bind with inorganic iron (nominally Fe^{3+}) in acidified subphases, with a binding response that differs significantly from that reported for the binding of simple mono- and divalent ions described previously in the literature. The cumulative evidence indicates that, despite the EDTA-like headgroup of Ace(18)-2-Ace(18), trivalent iron binding occurs through a nonspecific adsorption rather than a 1:1 chelation and that the binding is accompanied by compaction of the monolayer, as well as relatively small conformational changes to the constituent surfactant molecules. As has been reported with other surfactant monolayers in the literature, the speciation of the bound Fe^{3+} is complex and likely occurs as iron hydroxide clusters of the general formula $Fe_x(OH)_y^{(3x-y)+}$.

Acknowledgements Financial support for this work has been provided by the Natural Sciences and Engineering Research Council, the Canadian Foundation for Innovation, and the University of Saskatchewan. NSF's ChemMatCARS Sector 15 is supported by the Divisions of Chemistry (CHE) and Materials Research (DMR), National Science Foundation, under grant number NSF/CHE-1834750. Use of the Advanced Photon Source, an Office of Science User Facility operated for the U.S. Department of Energy (DOE) Office of Science by Argonne National Laboratory, was supported by the U.S. DOE under Contract No. DE-AC02-06CH11357.

Conflict of Interest The authors declare that they have no conflict of interest.

References

Alami, E., Beinert, G., Marie, P., & Zana, R. (1993) Alkanediyl-α,-ω-bis(dimethylalkylammonium bromide) surfactants. 3. Behavior at the air-water interface. *Langmuir*, **9**:1465–1467. https://doi.org/10.1021/la00030a006

Albert, C. T., & Douglas, V. (Eds.), *X-ray Data Booklet* (2nd ed.), Lawrence Berkeley National Laboratory (2001). https://xdb.lbl.gov/

Arakaki, A., Webb, J., & Matsunaga, T. (2003) A novel protein tightly bound to bacterial magnetic particles in Magnetospirillum magneticum strain AMB-1. *Journal of Biological Chemistry*, **278**: 8745–8750. https://doi.org/10.1074/jbc.M211729200

Aroti, A., Leontidis, E., Maltseva, E., & Brezesinski, G. (2004) Effects of hofmeister anions on DPPC langmuir monolayers at the air-water Interface. *Journal of Physical Chemistry B*, **108**: 15238–15245. https://doi.org/10.1021/jp0481512

Brzozowska, A. M., Mugele, F., & Duits, M. H. G. (2013) Stability and interactions in mixed monolayers of fatty acid derivatives on artificial sea water. *Colloids and Surfaces A: Physicochemical and Engineering Aspects*, **433**:200–211. https://doi.org/10.1016/j.colsurfa.2013.04.062

Bu, W., Mihaylov, M., Amoanu, D., Lin, B., Meron, M., Kuzmenko, I., … Schlossman, M. L. (2014) X-ray studies of interfacial strontium Extractant complexes in a model solvent extraction system. *The Journal of Physical Chemistry B*, **118**:12486–12500. https://doi.org/10.1021/jp508430e

Casper, C. B., Verreault, D., Adams, E. M., Hua, W., & Allen, H. C. (2015) Surface potential of DPPC monolayers on concentrated aqueous salt solutions. *The Journal of Physical Chemistry B*, **120**: 2043–2052. https://doi.org/10.1021/acs.jpcb.5b10483

Harris, D. C. (2010) *Quantitative chemical analysis* (8th ed.). New York: W.H. Freeman.

Islam, M. N., Bhattacharjee, D., & Hussain, S. A. (2008) Monolayer characteristics of pyrene mixed with stearic acid at the air-water interface. *Surface Review and Letters*, **15**:287–293. https://doi.org/10.1142/s0218625x08011378

Kang, Y. S., Lee, D. K., Lee, C. S., & Stroeve, P. (2002) In situ observation of domain structure in monolayers of arachidic acid/γ-Fe_2O_3 nanoparticle complexes at the air/water Interface. *Journal of Physical Chemistry B*, **106**:9341–9346. https://doi.org/10.1021/jp014484c

Kumar, N., & Tyagi, R. (2014) Industrial applications of dimeric surfactants: A review. *Journal of Dispersion Science and Technology*, **35**:205–214. https://doi.org/10.1080/01932691.2013.780243

Kumar, N., & Tyagi, R. (2015) Synthesis of anionic carboxylate dimeric surfactants and their interactions with electrolytes. *Journal of Taibah University for Science*, **9**:69–74. https://doi.org/10.1016/j.jtusci.2014.06.005

Leontidis, E., Christoforou, M., Georgiou, C., & Delclos, T. (2014) The ion-lipid battle for hydration water and interfacial sites at soft-matter interfaces. *Current Opinion in Colloid and Interface Science*, **19**:2–8. https://doi.org/10.1016/j.cocis.2014.02.003

Lopez-Moreno, R., Fernandez-Vivas, A., Valverde-Tercedor, C., Azuaga Fortes, A. I., Atienza, S. C., Rodriguez-Navarro, A. B., … Jimenez-Lopez, C. (2017) Magnetite nanoparticles biomineralization in the presence of the Magnetosome membrane protein MamC: Effect of protein aggregation and protein structure on magnetite formation. *Crystal Growth and Design*, **17**:1620–1629. https://doi.org/10.1021/acs.cgd.6b01643

Lv, J., & Qiao, W. (2015) Unusual pH-regulated surface adsorption and aggregation behavior of a series of asymmetric gemini amino-acid surfactants. *Soft Matter*, **11**:2577–2585. https://doi.org/10.1039/c5sm00041f

Lv, J., Qiao, W., & Xiong, C. (2014) Synthesis and surface properties of a pH-regulated and pH-reversible anionic Gemini surfactant. *Langmuir*, **30**:8258–8267. https://doi.org/10.1021/la5016669

Menger, F. M., & Keiper, J. S. (2000) Gemini surfactants. *Angewandte Chemie, International Edition*, **39**:1907–1920. https://doi.org/10.1002/1521-3773(20000602)39:11<1906::AID-ANIE1906>3.0.CO;2-Q

Michel, F. M., Ehm, L., Antao, S. M., Lee, P. L., Chupas, P. J., Liu, G., … Parise, J. B. (2007) The structure of ferrihydrite, a nanocrystalline material. *Science*, **316**:1726–1729. https://doi.org/10.1126/science.1142525

Mirabello, G., Lenders, J. J. M., & Sommerdijk, N. A. J. M. (2016) Bioinspired synthesis of magnetite nanoparticles. *Chemical Society Reviews*, **45**:5085–5106. https://doi.org/10.1039/C6CS00432F

Persson, I. (2018) Ferric chloride complexes in aqueous solution: An EXAFS study. *Journal of Solution Chemistry*, **47**:797–805. https://doi.org/10.1007/s10953-018-0756-6

Petty, M. C. (1996) *Langmuir-Blodgett films: An introduction*. Cambridge, England: Cambridge University Press.

Rehman, J., Ponce, C. P., Araghi, H. Y., & Paige, M. F. (2017a) Cation binding properties of an anionic gemini surfactant monolayer. *Colloids and Surfaces A: Physicochemical and Engineering*

Aspects, **522**:536–543. https://doi.org/10.1016/j.colsurfa.2017.03.039

Rehman, J., Sowah-Kuma, D., Stevens, A. L., Bu, W., & Paige, M. F. (2017b) Mixing behavior in binary anionic gemini surfactant-perfluorinated fatty scid langmuir monolayers. *Langmuir*, **33**: 10205–10215. https://doi.org/10.1021/acs.langmuir.7b02585

Rehman, J., Sowah-Kuma, D., Stevens, A. L., Bu, W., & Paige, M. F. (2019) Immiscible anionic gemini surfactant-perfluorinated fatty acid langmuir monolayer films. *Langmuir*, **35**:10551–10560. https://doi.org/10.1021/acs.langmuir.9b01554

Shah, D. O., & Schulman, J. H. (1965) Binding of metal ions to monolayers of lecithins, plasmalogen, cardiolipin, and dicetyl phosphate. *Journal of Lipid Research*, **6**:341–349.

Stefansson, A. (2007) Iron(III) hydrolysis and solubility at 25°C. *Environmental Science and Technology*, **41**:6117–6123. https://doi.org/10.1021/es070174h

Sung, W., Krem, S., & Kim, D. (2018) Binding of trivalent ions on fatty acid Langmuir monolayer: Fe3+ versus La3+. *The Journal of Chemical Physics*, **149**:163304/1–163304/7. https://doi.org/10.1063/1.5028296

Tyrode, E., & Corkery, R. (2018) Charging of carboxylic acid monolayers with monovalent ions at low ionic strengths: Molecular insight revealed by vibrational sum frequency spectroscopy. *Journal of Physical Chemistry C*, **122**:28775–28786. https://doi.org/10.1021/acs.jpcc.8b09505

Uebe, R., & Schueler, D. (2016) Magnetosome biogenesis in magnetotactic bacteria. *Nature Reviews Microbiology*, **14**:621–637. https://doi.org/10.1038/nrmicro.2016.99

Wang, W., Kuzmenko, I., & Vaknin, D. (2014) Iron near absorption edge X-ray spectroscopy at aqueous-membrane interfaces. *Physical Chemistry Chemical Physics*, **16**:13517–13522. https://doi.org/10.1039/c4cp00657g

Wang, W., Zhang, H., Feng, S., San Emeterio, J., Mallapragada, S., & Vaknin, D. (2016) Iron ion and iron hydroxide adsorption to charge-neutral phosphatidylcholine templates. *Langmuir*, **32**: 7664–7670. https://doi.org/10.1021/acs.langmuir.6b01851

Wani, F. A., Amaduddin, A. B., et al. (2019) Synthesis of novel Benzimidazolium Gemini surfactants and evaluation of their *anti-Candida* activity. *ACS Omega*, **4**:11871–11879. https://doi.org/10.1021/acsomega.9b01056

Wattebled, L., & Laschewsky, A. (2007) New anionic gemini surfactant based on EDTA accessible by convenient synthesis. *Colloid and Polymer Science*, **285**:1387–1393. https://doi.org/10.1007/s00396-007-1697-6

Wen, Y.-C., Zha, S., Liu, X., Yang, S., Guo, P., Shi, G., … Tian, C. (2016) Unveiling microscopic structures of charged water interfaces by surface-specific vibrational spectroscopy. *Physical Review Letters*, **116**:016101/1–016101/5. https://doi.org/10.1103/PhysRevLett.116.016101

Zana, R. (2002) Dimeric and oligomeric surfactants. Behavior at interfaces and in aqueous solution: A review. *Advances in Colloid and Interface Science*, **97**:205–253. https://doi.org/10.1016/S0001-8686(01)00069-0

Zhao, W., Song, K., Chen, Y., Wang, H., Liu, Z., Shi, Q., … Wang, Y. (2017) Aggregation of a cationic Gemini surfactant with a chelating molecule and effects from calcium ions. *Langmuir*, **33**: 12719–12728. https://doi.org/10.1021/acs.langmuir.7b03137